nature nanotechnology

SUPPLEMENTARY INFORMATION

https://doi.org/10.1038/s41565-019-0520-0

In the format provided by the authors and unedited.

Dielectric disorder in two-dimensional materials

Archana Raja[1,10,11]*, Lutz Waldecker[2,3,11], Jonas Zipfel[4], Yeongsu Cho[5], Samuel Brem[6], Jonas D. Ziegler[4], Marvin Kulig[4], Takashi Taniguchi[7], Kenji Watanabe[7], Ermin Malic[6], Tony F. Heinz[2,3], Timothy C. Berkelbach[8,9] and Alexey Chernikov[4]*

[1]Kavli Energy NanoScience Institute, University of California Berkeley, Berkeley, CA, USA. [2]Department of Applied Physics, Stanford University, Stanford, CA, USA. [3]SLAC National Accelerator Laboratory, Menlo Park, CA, USA. [4]Department of Physics, University of Regensburg, Regensburg, Germany. [5]Department of Chemistry and James Franck Institute, University of Chicago, Chicago, IL, USA. [6]Department of Physics, Chalmers University of Technology, Gothenburg, Sweden. [7]National Institute for Materials Science, Tsukuba, Ibaraki, Japan. [8]Department of Chemistry, Columbia University, New York, NY, USA. [9]Center for Computational Quantum Physics, Flatiron Institute, New York, NY, USA. [10]Present address: The Molecular Foundry, Lawrence Berkeley National Laboratory, Berkeley, CA, USA. [11]These authors contributed equally: Archana Raja, Lutz Waldecker. *e-mail: araja@lbl.gov; alexey.chernikov@regensburg.de

Dielectric disorder in two-dimensional materials

Archana Raja*,* Lutz Waldecker*, Jonas Zipfel, Yeongsu Cho, Samuel Brem, Jonas D. Ziegler, Marvin Kulig, Takashi Taniguchi, Kenji Watanabe, Ermin Malic, Tony F. Heinz, Timothy C. Berkelbach, and Alexey Chernikov†

CONTENTS

* archana.raja@berkeley.edu
† alexey.chernikov@ur.de

1. SAMPLE PREPARATION

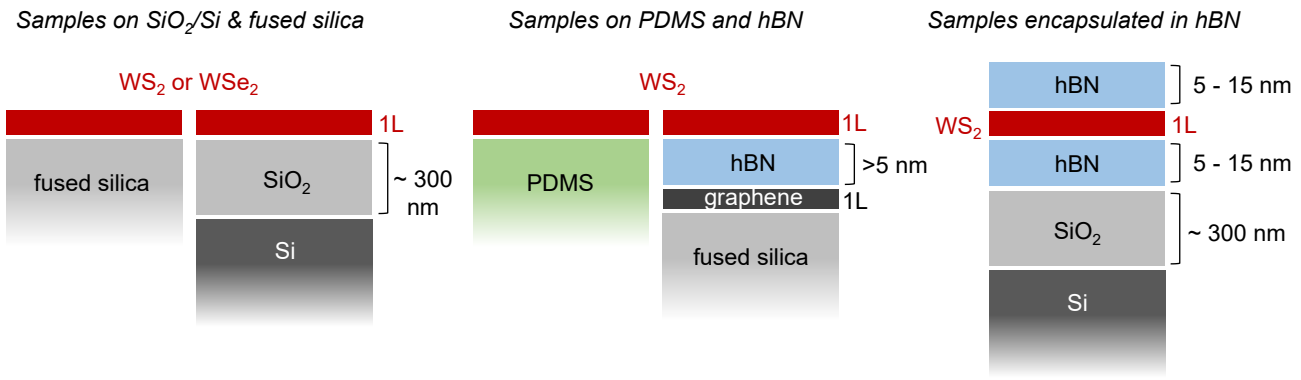

FIG. S1. **Schematic overview of the studied sample structures.**

Samples on SiO_2/Si and fused silica substrates: The monolayer WS_2 and WSe_2 samples used for obtaining statistics of the exciton linewidths at cryogenic temperatures were directly exfoliated from commercially available bulk crystals (obtained from "2Dsemiconductors" and "HQgraphene") either onto SiO_2/Si or fused silica substrates. No additional processing was applied and the samples were studied in their pristine as-exfoliated state.

Samples on PDMS and hBN: The monolayer WS_2 samples for the comparative study on polydimethylsiloxane (PDMS) and hexagonal boron nitride (hBN) substrates were produced from commercially available bulk WS_2 crystals (obtained from "HQgraphene"). First, crystals on scotch tape were directly exfoliated onto PDMS. Subsequently, samples on hBN were produced by direct exfoliation of separate hBN and WS_2 flakes onto PDMS and then stamped onto graphene covered fused silica substrates using the dry-transfer method from Ref [1]. The fabrication was followed by an annealing step at temperatures of 120-150°C for 1-2 hours in vacuum. The datapoints in Fig. 3 (b) in the main text are obtained from 38 individual positions on 7 different samples (hBN) and from 21 individual positions on 9 samples (PDMS).

Samples encapsulated in hBN: To obtain hBN-encapsulated samples, thin hBN flakes were first exfoliated on PDMS from bulk crystals (provided by T. Taniguchi and K. Watanabe, NIMS), stamped on a 100°C preheated SiO_2/Si substrate at ambient conditions, and subsequently annealed in high vacuum at 150°C for 4-5 hours. Monolayer WS_2 or WSe_2 flakes, exfoliated on PDMS, were then stamped on top of the hBN layers at 70°C substrate temperature and ambient conditions. Samples with WSe_2 were subsequently annealed again in high vacuum at 150°C for 4-5 hours, followed by the stamping of a thin hBN layer on top at 70°C substrate temperature. The resulting hBN-WSe_2-hBN heterostructure was then annealed again in high vacuum at 150°C for 4-5 hours. In case of WS_2, the structure was covered by hBN without any additional annealing.

We note that in our experience the source of the hBN crystals (NIMS, Tsukuba) turned out to be crucial for the successful encapsulation of monolayer TMDCs. On average, the procedure yielded samples with sufficiently large homogeneous areas (>50 μm^2) with narrow ground and excited state exciton resonances in more than roghly 60% of the produced encapsulated flakes. An important part of the preparation was the heating of the substrates and samples during a slow and steady mechanical transfer. This should allow surface adsorbates to move and to be pushed to accumulate in small pockets or at the sample edges by the strong van-der-Waals forces between layers. Together with the high quality of the used hBN, it leads to highly reproducible, clean and homogeneous interlayer contact in the remaining areas with homogeneous dielectric environment, as large as many 100's of μm^2 or more in the best samples. As a result of this procedure however, samples may also feature residual large-scale inhomogeneity with both areas of low disorder, where interlayer contact is good, and high disorder, where adsorbates are accumulated between layers, as further discussed in connection with the spatial reflectance mapping. In case of WSe_2, annealing after each individual layer deposition might even further improve the yield of samples with suppressed dielectric disorder. In contrast to that, the WS_2 samples are treated more carefully with respect to heating, as discussed above, since exposure to high temperature seemed to strongly influence sample quality.

2. REFLECTANCE SPECTROSCOPY

Optical reflectance spectroscopy was performed on several setups using similar equipment and measurement procedures. In these experiments, the light from a spectrally broadband tungsten-halogen lamp was focused by a 40x, NA= 0.6 objective onto the sample. The resulting spot sizes were typically in the range of one to a few micrometers and the integrated incident power on the sample was on the order of several 100's of nW or below. The reflected light was spectrally dispersed in a grating spectrometer and subsequently detected by a cooled charge-coupled-device (CCD) camera. The count accumulation time of an individual frame was usually chosen close to the saturation threshold of the CCD chip, followed by subsequent integration over 10's to 100's of frames to optimize signal-to-noise ratio. The data in Fig. 3 of the main text were taken at room temperature and under ambient pressure. Spectra collected at cryogenic temperature were measured on samples mounted in an optical microscopy cryostat cooled either by liquid nitrogen or liquid helium.

In the individual measurements, the reflectance signal was obtained both from a sample (R_{sample}) and a suitable substrate reference ($R_{\mathrm{substrate}}$) in close spatial proximity and in quick succession for optimal stability. An additional background measurement (BG) was then taken without illuminating the sample. The raw data were then combined to obtain a reflectance contrast spectrum R_C from $R_C = (R_{\mathrm{sample}} - R_{\mathrm{substrate}})/(R_{\mathrm{substrate}} - BG)$. It corresponds to the change of reflectance of the studied sample compared to the reflectance of the substrate and normalized by the latter. On transparent substrates, such as fused silica (e.g., see Fig. 2 in the main manuscript) this quantity is roughly proportional to the optical absorption when the reflectance contrast is not too high, being below or close to unity. For more complex structures, such as SiO_2/Si substrates or additional layers in a heterostructure (e.g., see Fig. 4 in the main manuscript), the overall shape of the spectra is strongly affected by multi-layer interference effects.

As an example, the data taken on a WS_2 monolayer encapsulated in thin layers of hBN on a SiO_2/Si substrate is presented in Fig. S2. As measured counts from the sample and substrate are shown in Fig. S2 (a) averaged over 100 frames with a 30 ms integration time for an individual frame. The corresponding background noise largely determined by the dark counts of the CCD is presented in the inset for comparison. Fig. S2 (b) illustrates the resulting reflectance contrast and its first derivative with respect to the photon energy. Here, the derivative is taken directly from the spectrum data. In case of broader and weaker features, smoothing via adjacent averaging method (in analogy to pixel binning) might be applied before and/or after the derivative is taken. The interval is then usually limited to the range of 5-10 meV and the averaging is also taken into account for the estimation of the peak parameters in the subsequent analysis.

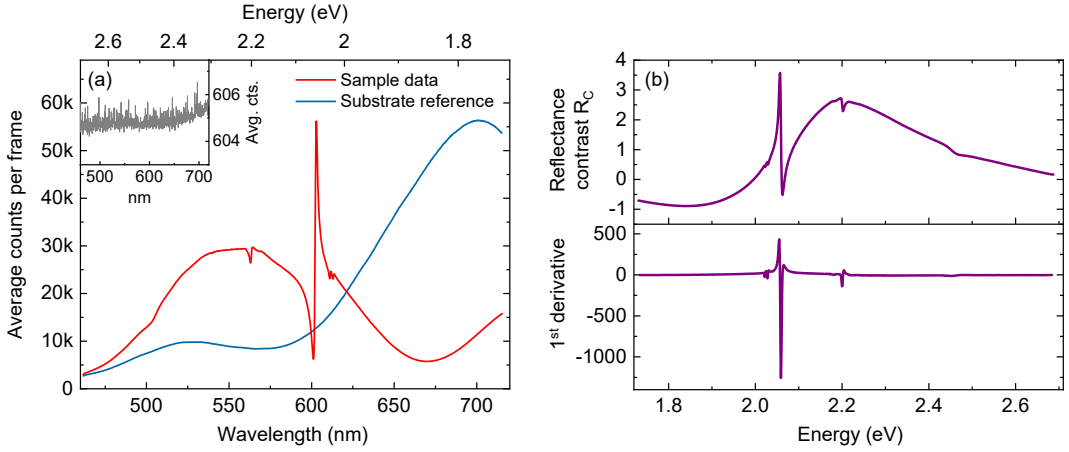

FIG. S 2. **Reflectance contrast spectroscopy.** (a) As-measured counts of the reflected light from an hBN-encapsulated WS_2 monolayer sample and SiO_2/Si substrate reference, averaged over 100 individual frames, as a function of wavelength. Background data acquired in the absence of the whitelight source is presented in the inset. (b) Resulting reflectance contrast spectrum R_C with respect to the SiO_2/Si reflectance (top panel) and the corresponding first derivative as functions of photon energy (bottom panel).

3. DATA ANALYSIS

To analyze the exciton resonances quantitatively, we construct a model dielectric function from a sum of inhomogeneously broadened Lorentz oscillators, each representing one of the main absorption features:

$$\varepsilon(E) = \varepsilon_b + \sum_1^n (L_n * G_n), \tag{1}$$

where $L_n * G_n$ denotes the convolution of complex Lorentzian and Gaussian lineshapes. In practice, the inhomogeneously broadened oscillators are implemented by a Faddeeva function F [2].

$$F(z) = \exp(-z^2) \cdot \mathrm{erfc}(-iz) \tag{2}$$

The dielectric function can then be expressed in terms of F:

$$\varepsilon(E) = \varepsilon_b + \sum_1^n f_n \frac{2i\sqrt{\pi \ln(2)}}{w_{G,n}} \cdot F\left(i \left[\sqrt{\ln(2)} \frac{w_{L,n}}{w_{G,n}} - 2i\sqrt{\ln(2)} \frac{E - E_n}{w_{G,n}} \right] \right), \tag{3}$$

where, E_n and f_n represent the peak energy and oscillator strength of the n-th individual resonance. The latter is determined by the light-matter coupling and contributes to the total linewidths of absorption- or emission-type features. $w_{L,n}$ denotes the non-radiative homogenous broadening (Lorentzian FWHM) and $w_{G,n}$ the inhomogeneous (Gaussian FWHM) contribution. The main advantage of the model is the explicit distinction between homogeneous and inhomogeneous broadening on the level of the dielectric response. As an approximation, a series of Lorentz resonances can also be used:

$$\varepsilon(E) = \varepsilon_b + \sum_1^n \frac{f_n}{E_n^2 - E^2 - iE\Gamma_{nr}} \tag{4}$$

where Γ_{nr} represents the total non-radiative homogeneous and inhomogeneous broadening. This description leads to deviations on the order of several meV in contrast to the Faddeeva model for the typical parameters in our study. It can be applied to estimate the total linewidth of the resonances with reasonable accuracy without specific assumptions considering the origins of the broadening. For the data in the main manuscript this approach was used for analyzing as-exfoliated samples for the histogram in Fig. 2 and hBN-encapsulated samples with strongly reduced inhomogeneous broadening, as presented in Fig. 4.

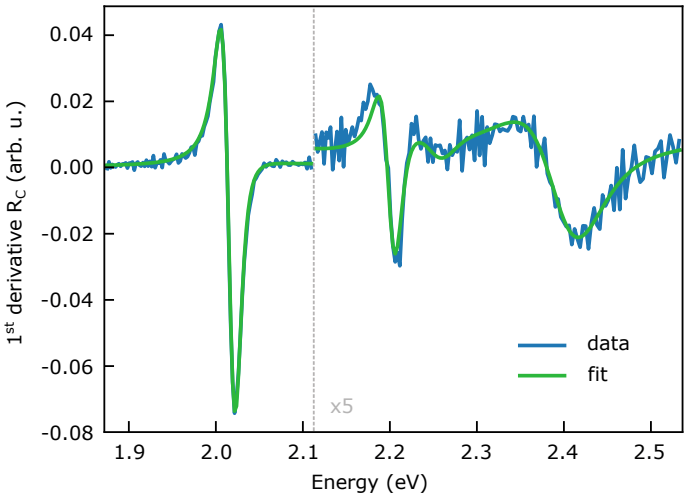

FIG. S3. **Reflectance data analysis.** Derivative of a reflectance contrast spectrum of a WS_2 monolayer with respect to the hBN/graphene/quartz substrate at room temperature (blue) and a least-square fit using the Faddeeva model (green, see text for details).

From the dielectric function, reflectance spectra (and their derivatives) for the respective sample geometries are then calculated. Propagation and interference effects from reflections at the interfaces between different layers are taken into account via a matrix-based formalism [3–5], and refractive indices of fused silica, hBN and graphite are taken from literature. For simplicity, normal incidence conditions are used in all cases. The model parameters are iteratively optimized to match the measured optical response. For the correlation plot in Fig. 3 of the main manuscript, optimization was done numerically to yield the best fit to the data using the full Faddeeva model. For better convergence and increased sensitivity to spectrally narrow resonance features, the difference of the derivative of the measured and simulated reflectance spectra are minimized.

In these fits, the Lorentzian linewidths (the homogeneous contribution) is kept constant. Based on theoretical expectations of homogeneous line broadening at room temperature due to interaction with phonons (see Sec. 6), we take a homogeneous linewidth of 20 meV for the ground state and for the first excited state as inputs to the fit. The Gaussian widths, together with the positions and amplitudes, are free fit parameters and directly yield the inhomogeneous broadening, spectral positions and oscillator strengths of the excitonic transitions. A representative fit is shown in Fig. S3 together with the measured reflectance contrast derivative.

4. CONTRIBUTIONS FROM HIGHER EXCITED STATES

Here, we briefly address the contributions from higher excited exciton states to measured reflectance spectra in as-exfoliated samples. While the transition of the first excited state, $n = 2$, dominates the optical response in the respective spectral range, signatures from higher lying states such as $n = 3$ are often observed. An exemplary spectrum of a WS_2 sample on SiO_2/Si substrate is presented in Fig. S4 (as well as in Fig. 4 (a) of the main manuscript). In the data, the signatures from the first three exciton states with $n = 1, 2, 3$ are observed. The detection of both $n = 2$ and $n = 3$ transitions is possible despite pronounced inhomogeneous broadening due to a sizable energy separation between these states of about 70 meV from reduced average dielectric screening in the absence of encapsulation. As consequence, the contribution of the $n = 3$ and even higher excited states to the $n = 2$ linewidth should be negligible. Nevertheless, in the discussion of as-exfoliated samples presented in the main manuscript we explicitly include at least the $n = 3$ state in the analysis, as its signature is frequently observed in the measurements. In addition, the $n = 3$ peak is comparably broad as $n = 2$, albeit we refrain from explicit consideration of the $n = 3$ linewidths due to close proximity of higher excited states and the bandgap.

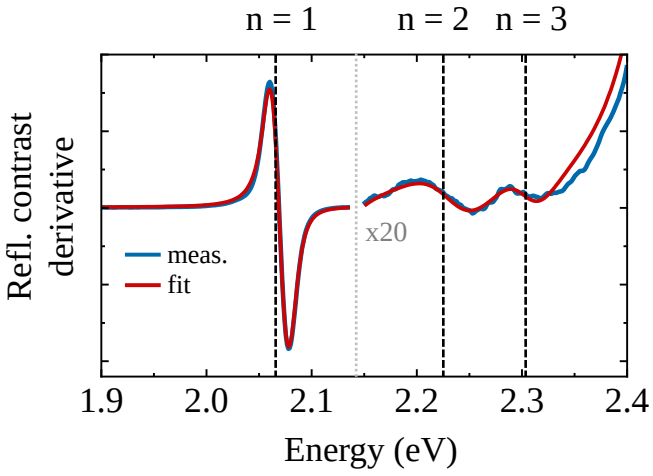

FIG. S4. **Contributions from higher excited states of the exciton.** Reflectance contrast derivative of an as-exfoliated WS_2 sample on SiO_2/Si substrate at liquid nitrogen temperature. The measured data is shown together with the fit from the multi-Lorentzian model. The energy positions of the exciton $n = 1, 2, 3$ resonances are indicated by dashed lines.

5. CORRELATIONS OF TOTAL LINEWIDTHS

In addition to the results presented in the main text, we show correlations of the *total* linewidths for the low-temperature and room-temperature sample statistics in Fig. S5 (a) and Fig. S5 (b), respectively. As an example, two typical spectra from hBN-supported samples are presented in Fig. S5 (c). The data shows that a small increase in the $n = 1$ linewidth of the sample B compared to A is indeed associated with a much broader $n = 2$ peak. In both cases we observe correlations between the total linewidths of the $n = 2$ and $n = 1$ exciton states, independent from any specific peak analysis procedure. In particular, the slopes of the trend lines through data on PDMS and hBN roughly follow those reported in the main manuscript. Here we note that the overall scattering in the low-temperature data is higher than for the room-temperature series, reflecting considerable variations of the samples' origin and potential modifications of the environment during cooling as well as possible pressure fluctuations in the cryostat.

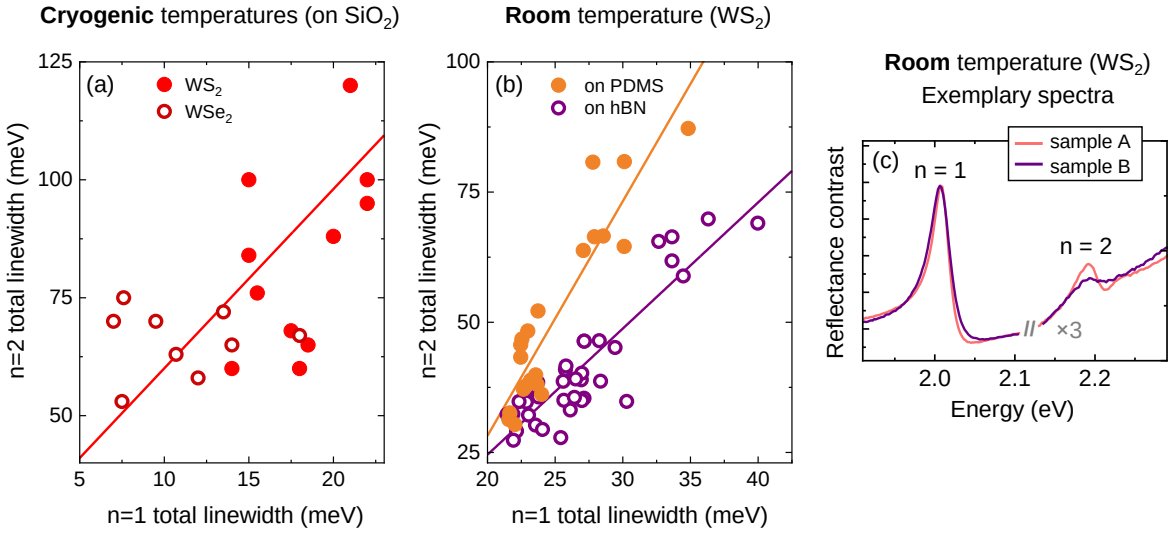

FIG. S 5. **Correlations of total exciton linewidths**. Correlation plots of the total linewidths of the $n = 1$ and $n = 2$ exciton states for studied WS_2 and WSe_2 samples at cryogenic temperatures on SiO_2 substrates (a) and the room-temperature results of the WS_2 sample series on hBN and PDMS substrates (b). (c) Reflectance contrast spectra of two WS_2 samples on hBN-substrate exhibiting different degrees of linewidth broadening.

6. HOMOGENEOUS BROADENING: EXPERIMENT AND THEORY

For the discussion and analysis of the exciton linewidths, it is necessary to consider the interplay between homogeneous and inhomogeneous contributions. This issue is of particular importance for the excited states of the exciton, which should experience additional scattering due to the relaxation into the ground state. In the following we expand the arguments provided in the main text from theoretical and experimental side and outline the basis of our interpretation in more detail.

6.0.1. Experimentally obtained limits for homogenous linewidths

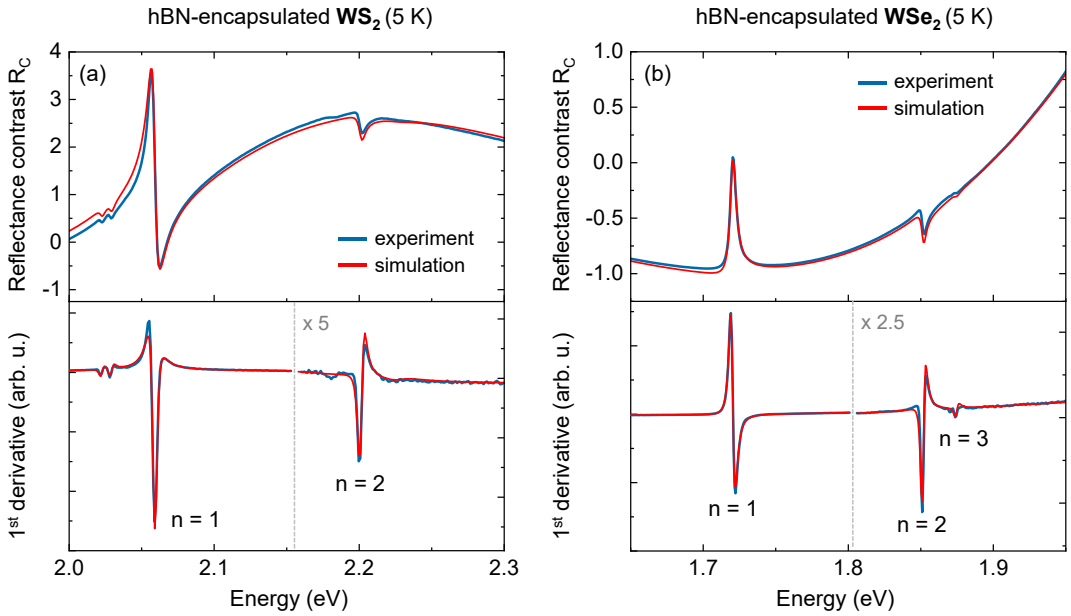

FIG. S6. **Exciton transitions in hBN-encapsulated samples**. Reflectance contrast spectra (top panels) and first derivatives (bottom panels) of hBN-encapsulated WS_2 (a) and WSe_2 (b) samples obtained at 5 K are presented with respect to the SiO_2/Si substrate reference. Simulation results using multi-Lorentzian parametrization of the dielectric function and transfer matrix method are shown for direct comparison. In the model, the top and bottom hBN capping layers are assumed to be of the same thickness of 8.8 nm and 14 nm for WS_2 and WSe_2 samples, respectively. The thickness of the SiO_2 layer is adjusted with values close to 300 nm.

In the experiment, it is reasonable to expect that an upper experimental limit for the homogeneous linewidth is provided by samples with the narrowest optical transitions and thus the smallest contributions from inhomogeneous broadening. For the studied WSe_2 and WS_2 monolayers, these are typically flakes fully encapsulated between thin hBN layers, measured at liquid helium temperature. Reflectance contrast spectra obtained at T = 5 K on two representative samples with narrow linewidths are presented in Fig. S6. The spectra are analyzed using an approximate approach outlined in Sec. 3 with each resonance being represented by a Lorentzian oscillator contributing to the energy-dependent complex dielectric function of the monolayer material with $f/(E_0^2 - E^2 - iE\Gamma_{nr})$. Here, E_0 is the resonance peak energy and f denotes the oscillator strength, providing radiative contribution to the total linewidth broadening of an absorption- or emission-type optical response, and the non-radiative broadening is labeled by Γ_{nr}. The results of the simulation are plotted in Fig. S6 on top of the experimental data for direct comparison.

The energy separation between $n = 1$ and $n = 2$ states of 143 meV in WS_2 and 131 meV in WSe_2 are in good agreement with recent reports [6–8] and match the expectations based on the changes in the dielectric screening due to encapsulation [9, 10]. We also note that the general assignment of the $n = 2$ resonance to the first excited state of the exciton in hBN-encapsulated samples is further collaborated by characteristic diamagnetic shifts in both WSe_2 [8] and WS_2 [11] as well as the observation of a higher, $n = 3$ state in the WSe_2 sample with reduced doping.

The extracted linewidths of the $n = 1$ exciton ground state and $n = 2$ excited state resonances are summarized in a table in Fig. S7. Presented are both non-radiative broadening parameters Γ_{nr} and the resulting total linewidths Γ_{tot}

obtained from the simulated absorption that include radiative contribution to broadening. The corresponding effective absorption spectra are shown in the right panel of Fig. S7 together with Lorentzian fits to the exciton resonances. The total linewidths of both $n = 1$ and $n = 2$ exciton states are similar and in the range of 5 meV. We also note that similar peak linewidths are observed in the photoluminescence spectra of the two samples. Moreover, the ground state broadening appears to be largely determined by the radiative coupling whereas the non-radiative scattering (potentially including some amount of inhomogeneous broadening) provides a smaller contribution. For the first excited state, however, the total linewidth is dominated by the non-radiative part. As previously discussed, these observations provide an upper limit for the relaxation rate of the $n = 2$ state towards $n = 1$ and strongly imply that the additional broadening of the excited states on the order of 60 - 100 meV observed in typical non-encapsulated samples at cryogenic temperatures is indeed inhomogeneous and does not stem from relaxation processes.

Exciton resonance	Non-radiative broadening Γ_{nr}	Total linewidth Γ_{tot}
n = 1 (WS_2)	1.7 meV	**5.8 meV**
n = 2 (WS_2)	5.0 meV	**5.2 meV**
n = 1 (WSe_2)	2.3 meV	**5.0 meV**
n = 2 (WSe_2)	3.5 meV	**3.8 meV**

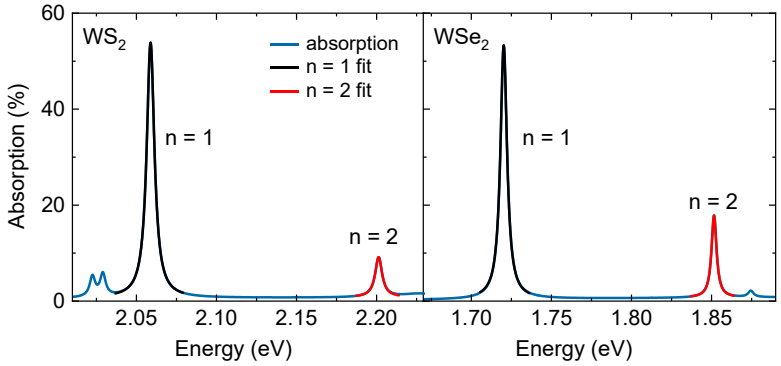

FIG. S 7. **Exciton broadening parameters extracted from experiments.** (Left panel) Summary of the extracted non-radiative and total linewidths of $n = 1$ and $n = 2$ exciton resonances in hBN-encapsulated WS_2 and WSe_2 samples at 5 K. (Right panels) Effective absorption spectra corresponding to the simulated response presented in Fig. S6.

At higher temperatures, however, the absorption of phonons becomes more likely and the homogeneous linewidth increases. The same samples presented in Figs. S6 and S7 show total linewidths close to 25 meV for WS_2 and 35 meV for WSe_2 at room temperature for both $n = 1$ and $n = 2$ resonances. The temperature dependence of WS_2 is illustrated in Fig. S8. Across the studied temperature range, the linewidths of excited states are thus very similar to that of the ground state. These findings are in good agreement with the results of microscopic calculations explicitly including light-matter coupling of the exciton states as well as intra- and intervalley exciton-phonon scattering [12], as discussed in more detail further below.

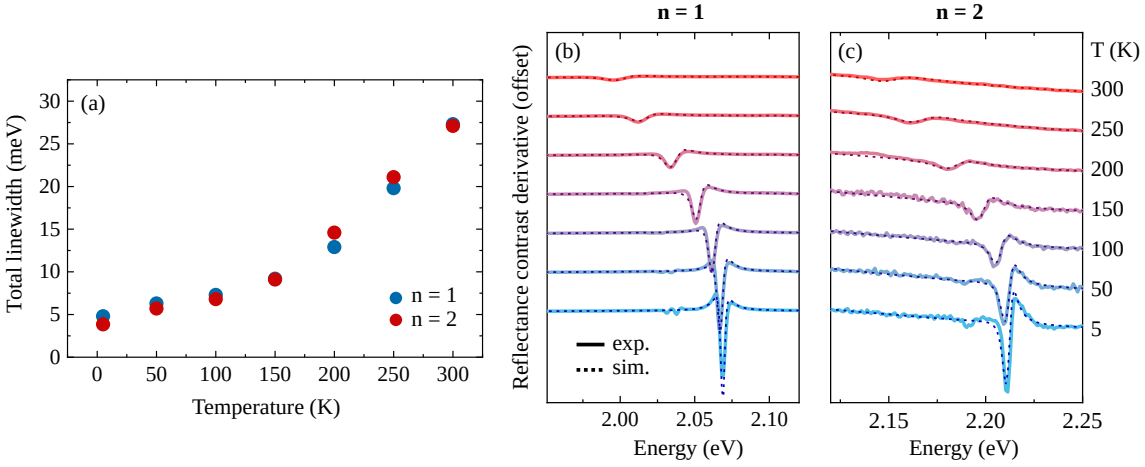

FIG. S 8. **Temperature dependent linewidths of exciton ground and excited states**. (a) Total linewidths of the $n = 1$ and $n = 2$ exciton states in hBN-encapsulated WS_2 as function of lattice temperature obtained from reflectance spectroscopy. Corresponding reflectance contrast derivatives including the fit curves (black dashed lines) are presented in (b) and (c), respectively.

6.0.2. *Theoretical calculations of homogenous broadening*

To assess the contributions from homogeneous broadening of the exciton states on the level of microscopic theory, the reflectance spectrum has been obtained via the semiconductor Bloch equations in the low density limit, which have been numerically solved based on material parameters for WS_2 from ab initio calculations [13–15]. The Coulomb interaction is treated on a Hartree-Fock level where the interaction strength is determined by the Rytova-Keldysh potential for thin films [16, 17]. In exciton basis the dielectric susceptibility of the monolayer can be written as [18]

$$\chi(\omega) = \frac{|d_{cv}|^2}{\epsilon_0} \sum_{\mu} \frac{|\Phi_\mu(r=0)|^2}{E_\mu - \hbar\omega - i\gamma_\mu}, \tag{5}$$

where the excitonic wave functions Φ_μ and the eigenenergies E_μ are determined by the Wannier equation[19]. Moreover, the strength of the optical response is scaled by the interband oscillator strength d_{cv} [20]. The line broadening γ_μ is microscopically calculated by taking into account the phonon scattering induced dephasing, which is obtained within a second-order Born-Markov approximation for exciton-phonon correlations in analogy to ref. [12]. Here we include intra- as well as intervalley scattering with acoustic and optical phonons across the whole excitonic Rydberg series [21] for intra- as well as intervalley excitons [19]. From the susceptibility χ we obtain the reflectance contrast of the monolayer on fused silica substrate.

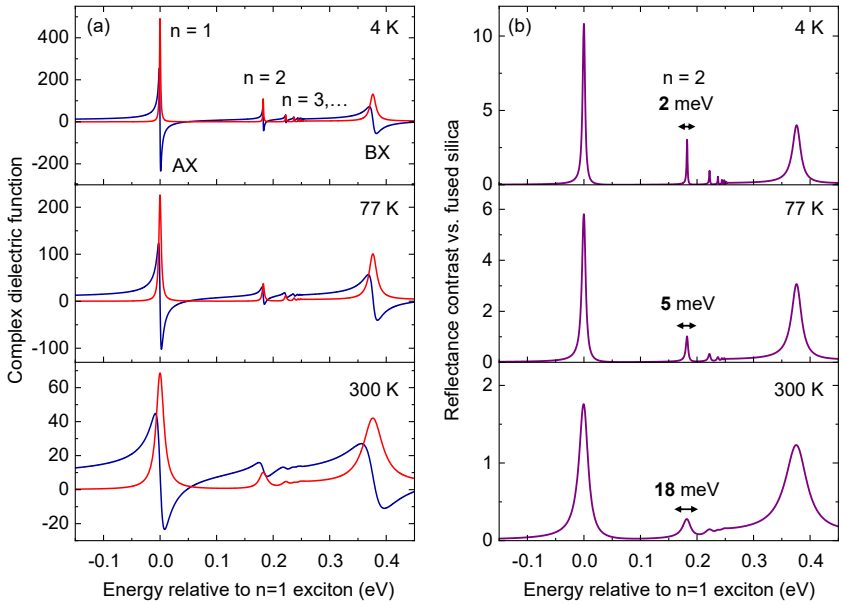

FIG. S 9. **Theoretical results of the exciton spectra with microscopically calculated linewidths from radiative and phonon-mediated broadening**. (a) Theoretically calculated dielectric functions of WS_2 monolayer for the lattice temperatures of 4 K (top), 77 K (middle), and 300 K (bottom). The exciton ground states corresponding to the spin-split A and B transitions are denoted by "AX" and "BX", respectively, and the series of the A exciton states is labeled by the principal quantum number $n = 1, 2, 3, ...$ (b) Corresponding reflectance contrast spectra for monolayers on fused silica substrates. The full-width-half-maximum linewidths of the $n = 2$ exciton resonances are indicated.

The resulting dielectric functions and corresponding reflectance contrast spectra are presented in Fig. S9 (a) and Fig. S9 (b), respectively, for the lattice temperatures of 4, 77, and 300 K. The spectra include contributions from A and B exciton series and continuum states, excluding higher energy transitions such as the C-band at about 2.9 eV and above. The data is presented relative to the energy of the A exciton ground state. For all temperatures, the linewidths of the $n = 2$ and $n = 1$ states are found to be comparable, with full-width-half-maximum values close to 20 meV at room temperature. While the scattering from the 1s state to 2s state is very inefficient due to the large required momentum transfer, the additional relaxation channels from the $n = 2$ towards the lower lying $2p$ excitons contributes to the increase of the linewidth. However, the overall exciton-phonon scattering is less efficient for the $n = 2$ state. The main reason is the larger spatial extent of the $n = 2$ orbital compared to $n = 1$. The resulting reduction of the orbital overlap in momentum space gives rise to a reduced scattering efficiency for the n=2 state.

For liquid nitrogen and liquid helium temperatures, in particular, the total homogenous broadening of the $n = 2$ state is on the order of 3-5 meV. It matches well the measured total linewidths of the hBN-encapsulated samples and is much smaller than the inhomogeneous widths of 60 - 100 meV in as-exfoliated samples from dielectric disorder. Interestingly, due to the smaller radiative contribution, the intrinsic broadening of the $n = 2$ resonance is even slightly smaller than that of the $n = 1$ state, as also implied by the measurements of encapsulated samples at 4 K, discussed in the previous section (see Fig. S7). Similar results and conclusions for temperature dependent broadening of exciton states in WSe_2 mononlayers are reported in Ref. [22].

7. CALCULATIONS OF COULOMB RENORMALIZATION

The environmentally sensitive optical properties are calculated following Ref. [23]. We treat a WS_2 monolayer as an infinite slab with a thickness d and dielectric constant ε surrounded by a continuum of dielectric constant ε_{ext}. Charges are considered to occupy only the center of the WS_2 slab and experience a modified screening depending on the dielectric environment. The resulting screened Coulomb interaction between two elementary charges is obtained by the method of images,

$$W(\rho) = \frac{e^2}{\varepsilon\rho} + \frac{2e^2}{\varepsilon}\sum_{n=1}^{\infty}\frac{\xi^n}{\{\rho^2 + (nd)^2\}^{1/2}}, \tag{6}$$

where ρ is the in-plane distance between two charges and $\xi = (\varepsilon - \varepsilon_{\text{ext}})/(\varepsilon + \varepsilon_{\text{ext}})$. The change in the band gap of the monolayer compared to its value in the bulk is evaluated as the sum of the self-energy of a hole for the valence band and an electron for the conduction band,

$$\delta\Sigma_{c/v} = \pm\frac{1}{2}\lim_{\rho\to 0}\left(W(\rho) - \frac{e^2}{\epsilon\rho}\right), \tag{7}$$

where the second term indicates that the correction term is calculated by regarding the bulk material as the reference system. This leads to the environmentally sensitive monolayer band gap

$$E_{\text{g}}^{\text{mono}}(\varepsilon_{\text{ext}}) = E_{\text{g}}^{\text{bulk}} + \lim_{\rho\to 0}\left(W(\rho) - \frac{e^2}{\epsilon\rho}\right) = E_{\text{g}}^{\text{bulk}} + \frac{e^2}{\varepsilon d}\left\{2\tanh^{-1}(\xi) - \ln(1-\xi^2)\right\}. \tag{8}$$

For bulk WS_2, we use the literature value of $E_g = 2.01$ eV from Ref. [24], fixing the absolute bandgap energy at $\varepsilon_{ext} = 16.7$. To calculate the exciton states and their binding energies, we solve the Schrodinger equation with an effective mass Hamiltonian

$$\left[-\frac{1}{2\mu}\nabla_\rho^2 - W(\rho)\right]\Psi_n(\rho) = E_n^{\text{X}}(\varepsilon_{\text{ext}})\Psi_n(\rho), \tag{9}$$

where $W(\rho)$ is the same screened Coulomb interaction as given in Eq. (6) and μ is the reduced mass of the exciton. The material properties of monolayer WS_2 are taken from Ref. [25]: $\varepsilon = 16.7$, $d = 6.175$ Å, and $\mu = 0.16$. The eigenfunctions and eigenvalues of the exciton Hamiltonian are found via diagonalization in a basis of radial real-space grid points. Through its dependence on $W(\rho)$, the exciton binding energies are sensitive to the dielectric constant of the environment and the optical transition energies are given by

$$E_n(\varepsilon_{\text{ext}}) = E_{\text{g}}^{\text{mono}}(\varepsilon_{\text{ext}}) + E_n^{\text{X}}(\varepsilon_{\text{ext}}). \tag{10}$$

Here we note that the model we use to describe the environment by a uniform and static dielectric constant is the simplest one that captures the dielectric disorder effect. A more general, frequency dependent dielectric function can be in principle incorporated in these calculations to account for dynamical screening in both the TMDCs and their environment. The most important dynamical mechanisms to be considered should occur with a characteristic energy on the same scale as the exciton binding energies, i.e. 200 meV or more. While this energy scale is significantly larger than the phonon modes of the studied TMDC semiconductors, a number of common substrates exhibit phonon characteristic frequencies closer to this energy range. Therefore, a more complex, microscopic model that would include substrate phonon dynamics could potentially provide more detailed insights into a richer regime of the studied phenomena.

8. SPATIAL MAPPING OF DISORDER

8.1. Disorder on micrometer scales

To illustrate the effect of dielectric disorder on optically accessible spatial scales we have studied distinct scenarios arising in hBN-encapsulated WS_2 monolayer samples using reflectance spectroscopy mapping. As indicated in the top schematic of Fig. S10, a reflectance contrast spectrum was obtained for each position on the sample with a step size between 0.5 and 1 μm and a spot width on the order of 1.5 μm. Measurements on the SiO2/Si substrate were used as a reference. From each spectrum we extract the energies of the exciton ground state ($n = 1$) and the first excited state ($n = 2$) transitions using the fitting procedure described above and taking into account interference effects in the multi-layer structure. The energy separation of the two states Δ_{12} is proportional to the exciton binding energy E_b with a prefactor of about 1.3 for hBN-encapsulated flakes as recently shown for the case of WSe_2 [8] that is very similar to WS_2 with respect to both magnitude of the Coulomb effects and scaling of the exciton states [11, 26]. In general, Δ_{12} is a measure of the effective strength of the Coulomb interaction and is directly related to the environmental dielectric permittivity [10]. The freeparticle bandgap is then obtained from the sum of the transition energy of the $n = 1$ resonance and the binding energy. The bandgap is thus sensitive both to changes in the dielectric environment and to any additional fluctuations such as strain and doping.

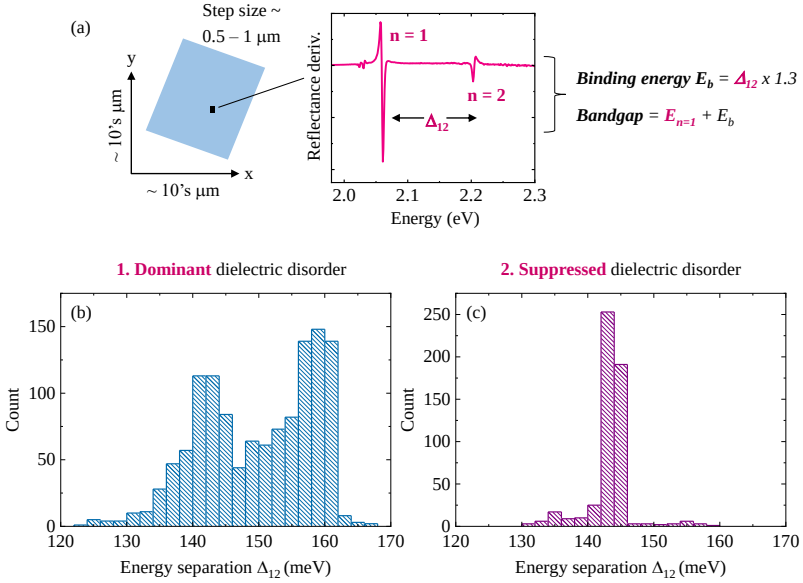

FIG. S 10. **Reflectance mapping spectroscopy of the exciton states.** (a) Schematic illustration of the reflectance spectroscopy mapping including a typical reflectance derivative spectrum of an hBN-encapsulated WS_2 monolayer sample. The exciton ground ($n = 1$) and first excited state ($n = 2$) resonances are detected and automatically fitted at each sample position using the Lorentzian peak model in the dielectric function, according to the procedure outlined in Sect. 3. The binding energy and the absolute bandgap position are then estimated from the difference between the exciton state energies Δ_{12} and by adding the obtained $n = 1$ binding energy to the transition energy of the $n = 1$ state, respectively. Histograms of the Δ_{12} values are presented in panels (b) and (c) for two different outcomes of the hBN-encapsulation, resulting either in pronounced fluctuations of the Coulomb interaction on a few-micrometer scale (a) or in a relatively high spatial homogeneity (b).

As an overview, two distinct cases are presented Figs. S10 (b) and (c), showing the histograms of Δ_{12} obtained from the spatial mapping of two different heterostructures. In the first case, we observe pronounced fluctuations of the exciton states separation Δ_{12} corresponding to spatial variations of the Coulomb interaction on few-micrometer scales. Here, the transfer of the WS_2 on top the hBN flake and the subsequent capping with a second hBN flake resulted in large spatial fluctuations, most probably related to the trapping of the adsorbates between the layers and thus non-ideal interlayer contact across large studied areas of several 100's of μm^2. The second case shows a scenario where the hBN-encapsulation was largely successful and resulted in nearly constant Δ_{12} energy separation across the studied flake with the area of roughly 200 μm^2. It corresponds to spatially independent average strength of the Coulomb interaction due to homogeneous dielectric environment. Detailed maps of both exciton transition and binding energies as well as the estimated bandgap energy are discussed in the following. An additional analysis of doping and strain fluctuations in the same samples based on spatial mapping is presented in Sect. 9.

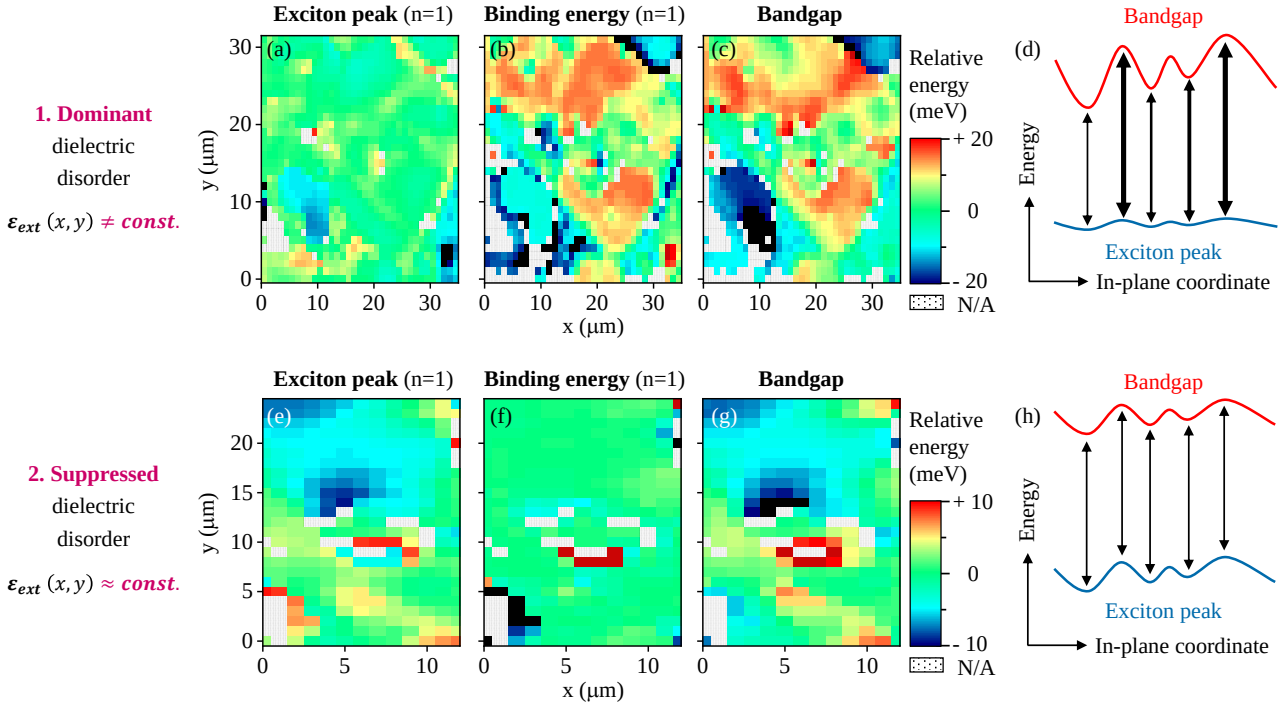

FIG. S11. **Spatial mapping of disorder in hBN/WS_2/hBN heterostructures based on reflectance measurements of exciton $n = 1$ and $n = 2$ resonances.** The extracted energy fluctuations of the exciton ground state resonance, exciton binding energy, and freeparticle bandgap position for a sample exhibiting dominant dielectric disorder effects are presented in (a), (b), and (c), respectively. A corresponding schematic illustrating the nature of the fluctuations consistent with the experimental data is shown in (d). Maps of a second sample with strongly suppressed dielectric fluctuations are presented in (e), (f), and (g) with a schematic illustration provided in (h).

8.1.1. Dominant dielectric disorder

The extracted energy fluctuations of the exciton ground state resonance, exciton binding energy, and freeparticle bandgap position obtained on the sample with pronounced dielectric fluctuations are presented in Figs. S11 (a), (b), and (c), respectively, corresponding to the data shown in the main manuscript. In this sample, the fluctuations of the exciton ground state transition energy are relatively small. In contrast to that, the exciton peak separation Δ_{12} (c.f. Fig. S10 (b)) and hence the exciton binding energy exhibit sizable variations in the range of 40 meV due to spatial inhomogeneity of the environmental screening. As a consequence, fluctuations of the freeparticle bandgap energy are strongly correlated with the exciton binding energy. It follows that dielectric variations are the predominant source of disorder on few-micrometer scales in the present heterostructure, as further illustrated in the schematic in Fig. S11 (d).

8.1.2. Suppressed dielectric disorder

Spatial maps of the exciton binding energy, and freeparticle bandgap from a heterostructure with suppressed dielectric disorder are presented in Figs. S11 (e), (f), and (g). In this case, we do not observe any sizable variations of the exciton peak separation Δ_{12} corresponding to an essentially constant value of the exciton binding energy across the studied area. Instead, the bandgap fluctuations closely follow the variations of the absolute energy of the exciton transition. The dielectric disorder is thus strongly reduced in this heterostructure as illustrated in Fig. S11 (h), with the remaining inhomogeneities stemming from sources not directly related to Coulomb renormalization effects, such as strain or doping, as further discussed in Sect. 9.

8.2. Spatial scales of disorder

In both cases discussed above we emphasize that the spatial scale of disorder accessible by analyzing only the peak energies in optical experiments is naturally limited by the resolution in the range of 1 μm. As discussed in the main manuscript, inhomogeneities on smaller spatial scales contribute to the spectral broadening of the resonances instead. Thus, the observation of either spatially fluctuating peak energies or inhomogeneously broadened ensemble depends on the averaged sample area in the experiment. That also determines the definition of the average value of ε_{ext} and its fluctuations $\Delta\varepsilon_{ext}$ in each specific case.

The influence of dielectric disorder on different scales is further illustrated using the heterostructures discussed above. In the first case, the fluctuations of the dielectric environment occur within several micrometers and are directly visible in the variations of the relative peak energies of the $n = 1$ and $n = 2$ exciton transitions. The consequences for the exciton binding energies and the free particle bandgap position can be thus directly visualized, as shown in Figs. S11 (b) and (c). In the second case, the dielectric fluctuations are strongly suppressed on the micrometer-scale, as illustrated by a nearly constant energy separation Δ_{12} of the exciton transitions within a few meV, presented as histogram in Fig. S10 (c) and as a map in Fig. S12 (a). However, residual fluctuations can still occur on much smaller spatial scales below the optical resolution. These can be inferred from the broadening of the resonances instead, following the discussion in the main manuscript (Fig. 3(b)) and extracted from individual reflectance specra, as indicated in Fig. S12 (b). Correlation of the non-radiative linewidths of $n = 1$ and $n = 2$ states is presented in Fig. S12 (c) as obtained by the peak fitting procedure from the spatially resolved reflectance mapping.

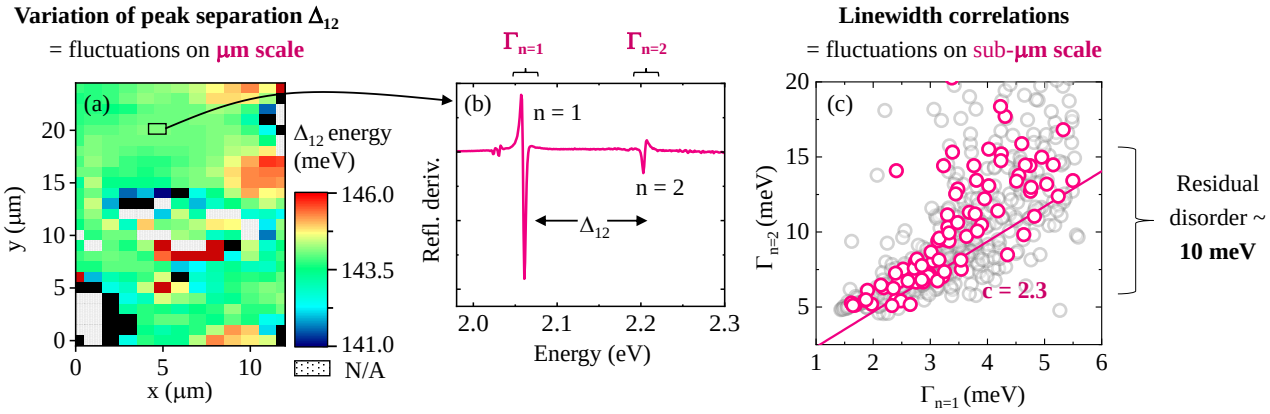

FIG. S 12. **Exciton state separation mapping and linewidths correlations for a sample with largely suppressed dielectric disorder**. (a) Spatial map of the $n = 1$ and $n = 2$ exciton peak separation Δ_{12} in the second sample with strongly suppressed dielectric disorder on micrometer scales (same as in lower panel of Fig. S11). (b) Typical reflectance contrast derivative spectrum used to extract the resonance linewidths via procedure outlined in Sect. 3. (c) Correlation plot of the non-radiative $n = 2$ linewidth as function of the non-radiative $n = 1$ linewidth. The gray circles represent the full data set and the pink ones correspond to every 6'th value for better readability.

Similar to the results discussed in the main manuscript we observe overall larger broadening of the $n = 2$ resonances compared to the $n = 1$ peaks. Moreover, the linewidths are correlated with a scaling factor consistent with the average screening provided by hBN-encapsulation. The broadening can be thus attributed to a small amount of residual dielectric disorder. In contrast to the nearly constant average screening on a few-micrometer scale, the spatial scale of these fluctuations is much smaller than the optical spot size. We also note that these fluctuations are about an order of magnitude smaller compared to what we commonly find in as-exfoliated samples on typical substrates, further motivating the use of hBN-encapsulation to mitigate and suppress dielectric disorder.

9. DOPING AND STRAIN FLUCTUATIONS

In addition to fluctuations of the environmental dielectric permittivity, common sources of inhomogeneities in van der Waals mono- and few-layer materials are non-uniform doping and strain. As discussed in the main manuscript, strain mainly affects the energies of the electron and hole bands, yet it has only a small effect in the range of 5-10 meV per percent strain on the binding energies of the exciton states [27]. In contrast to that, a sizable level of doping can strongly affect the relative positions of the exciton states and renormalize the bandgap [26]. In the previous Sect. 8 we have presented two cases with either pronounced or suppressed fluctuations of the dielectric screening. To determine the role of doping in these structures we have analyzed the signatures of trion resonances appearing in the spectra below the exciton ground state energy. The signal from the trion peaks, also labeled as attractive Fermi-polarons in the literature [28], is proportional to the density of free charge carrier in the low-to-intermediate doping regime.

9.1. Dominant dielectric disorder

First, we discuss the case with pronounced dielectric disorder. We have chosen three representative positions corresponding to different values of the exciton binding energy and bandgap position, as indicated in Fig. S13 (a). The corresponding reflectance derivative spectra are presented in Fig. S13 (b) together with the respective fit curves. Resonance energies of the trion states, the exciton ground and first excited states are indicated by dotted lines. The trion states appear as a peak doublet characteristic for electron doped W-based TMDCs [6, 29]. In all three spectra, the contributions from trion signatures are very similar. Neither the trion-exciton energy separation nor the oscillator strength correlate with the changes of the bandgap and exciton binding energies, as shown in Fig. S13 (c). Moreover, the oscillator strengths of the trion features are very weak, on the order of few percent of the neutral exciton resonance, indicating very low level of doping. Therefore, doping contributions to the observed changes in the exciton binding energies and bandgap position are negligible, leaving the fluctuations of the static screening as the dominant origin of the disorder in this sample.

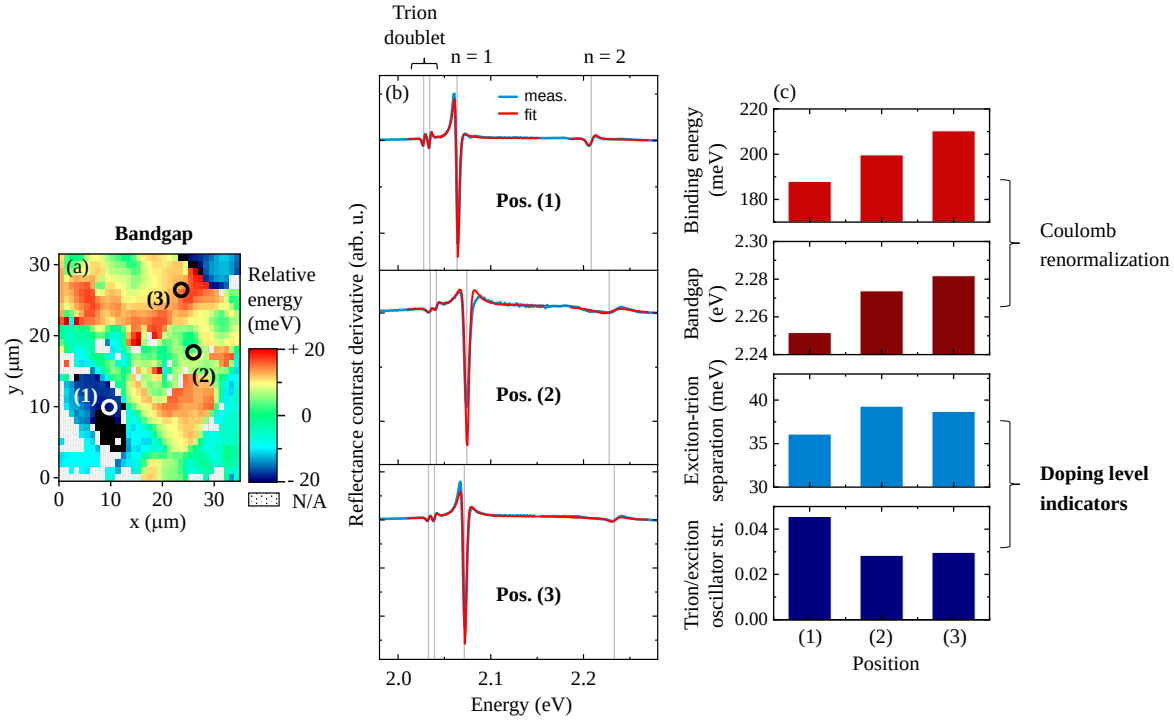

FIG. S13. **Representative analysis of dielectric effects and doping**. (a) Spatial map of the relative bandgap energies from an hBN-encapsulated WS_2 monolayer exhibiting pronounced fluctuations due to the changes of the local dielectric screening. (b) Individual reflectance contrast derivative spectra taken from three representative positions on the sample with different exciton binding energies and bandgap positions. Transition energies of the trion states, the exciton ground and first excited states are obtained from the fitting and indicated by dotted lines. (c) Corresponding exciton binding energies, absolute bandgap energies, energy separations of the lower-energy trion, and the relative oscillator strengths of the trion doublet compared to the exciton ground state from the three positions.

9.2. Suppressed dielectric disorder

As discussed in the previous section, the variations of the screening on micrometer scales are largely suppressed in this sample. As a consequence, alternative sources of disorder not related to static screening such as doping and strain should be considered. To study the local changes in doping density, we examine the relative contributions from the trion states to the optical spectra, as indicated in the left panel of Fig. S14 (a). The combined oscillator strength of the trion doublet relative to the ground state exciton is presented in the right panel of Fig. S14 (a) in comparison to variations of the exciton resonance, exciton binding energy and the bandgap energy, plotted in Fig. S14 (b), (c), and (d), respectively. Similar to the previous case, the oscillator strength of the trion is overall very weak across the sample. The variations, proportional to local fluctuations of the doping density, are also not correlated with the changes of the bandgap position. The influence of doping is thus negligible, leaving strain fluctuations a most probable origin of the residual fluctuations of the exciton and bandgap transition in this sample.

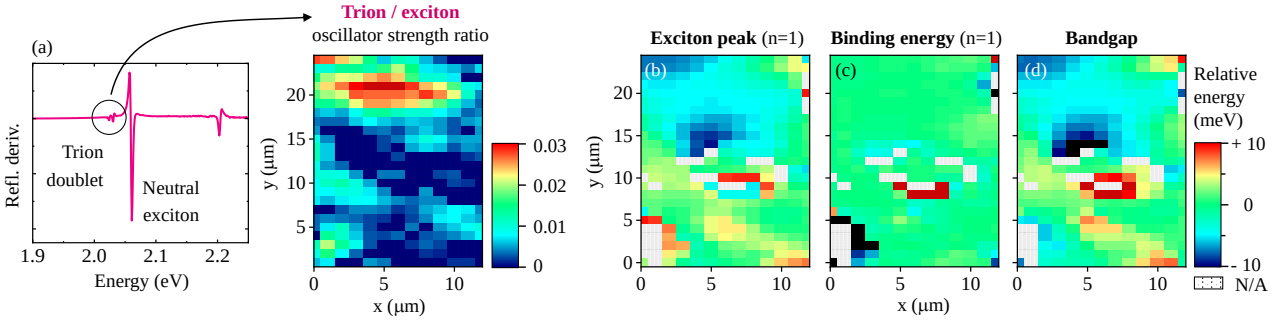

FIG. S 14. **Mapping of spectroscopic signatures of doping**. (a) Representative reflectance derivative spectrum with an indicated trion doublet (left panel) and a spatial map of its relative oscillator strength (right panel) obtained on the hBN-encapsulated WS_2 monolayer with suppressed dielectric disorder. (a-c) Corresponding spatial maps of the relative energy fluctuations of the exciton ground state resonance, exciton binding energy, and freeparticle bandgap position, respectively.

10. EXCITON DIFFUSION EXPERIMENTS

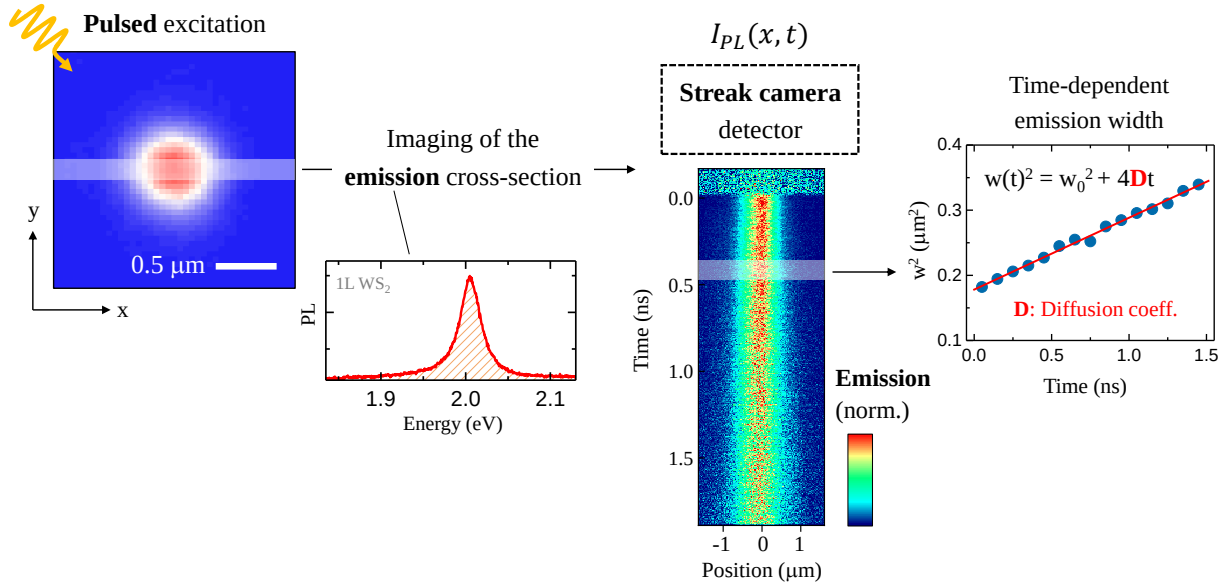

FIG. S 15. **Schematic illustration of the time-resolved imaging microscopy technique**. It includes typical results on WS_2 monolayer sample at room temperature and the analysis of the diffusion coefficient from time-dependent broadening of the emission profile. Parts of the presented data are reported in Ref. [30].

To illustrate the impact of disorder and its mitigation on the exciton propagation, we have performed a series of measurements using spatially- and time-resolved microscopy that was recently applied to study exciton diffusion in transition-metal dichalcogenide monolayers [30]. The main experimental method is illustrated in Fig. S15. We used a 100-fs pulsed Ti:sapphire laser with 80 MHz repetition rate centered at photon energy of 2.4 eV for excitation. The incident beam was focused on a small spot on the sample of about 0.5 μm in diameter by a 100x microscope objective. The emission cross-section was collected and imaged on a streak camera detector, providing temporal resolution along the y-axis. The x-axis corresponds to the spatial coordinate. Spatial luminescence profiles were then extracted at each time step and fitted by Gaussian peak functions. According to the solution of the diffusion equation in two dimensions, the slope of the time-dependent squared width is proportional to the diffusion coefficient with a prefactor of 4. For the data reported in the main manuscript, we studied a series of as-exfoliated and hBN-encapsulated WS_2 monolayer samples for direct comparison. All experiments were performed at room temperature and ambient conditions.

[1] Castellanos-Gomez, A. *et al.,* Deterministic transfer of two-dimensional materials by all-dry viscoelastic stamping. *2D Mater.* **1**, 11002 (2014).

[2] De Sousa Meneses, D., Brun, J.-F., Echegut, P., and Simon, P., Contribution of semi-quantum dielectric function models to the analysis of infrared spectra. *Appl. Spectr.* **58**, 969 (2004).

[3] Byrnes, S. J., `http://sjbyrnes.com/multilayer-film-optics-programs/`.

[4] Byrnes, S. J., Multilayer optical calculations. arXiv:1603.02720 (2016).

[5] Li, Y. *et al.*, Measurement of the optical dielectric function of monolayer transition-metal dichalcogenides: MoS_2, $MoSe_2$, WS_2, and WSe_2. *Phys. Rev. B* **90**, 205422 (2014).

[6] Courtade, E. *et al.*, Charged excitons in monolayer WSe_2: Experiment and theory. *Phys. Rev. B* **96**, 085302 (2017).

[7] Manca, M. *et al.*, Enabling valley selective exciton scattering in monolayer WSe_2 through upconversion. *Nature Commun.* **8**, 14927 (2017).

[8] Stier, A. V. *et al.*, Magnetooptics of exciton Rydberg states in a monolayer semiconductor. *Phys. Rev. Lett.* **120**, 057405 (2018).

[9] Stier, A. V., Wilson, N. P., Clark, G., Xu, X., and Crooker, S. A., Probing the influence of dielectric environment on excitons in monolayer WSe_2: Insight from high magnetic fields. *Nano Lett.* **16**, 7054 (2016).

[10] Raja, A. *et al.*, Coulomb engineering of the bandgap and excitons in two-dimensional materials. *Nature Commun.* **8**, 15251 (2017).

[11] Zipfel, J. *et al.*, Spatial extent of the excited exciton states in WS_2 monolayers from diamagnetic shifts. *Phys. Rev. B* **98**, 075438 (2018).

[12] Selig, M. *et al.*, Excitonic linewidth and coherence lifetime in monolayer transition metal dichalcogenides. *Nature Commun.* **7**, 13279 (2016).

[13] Kormányos, A. *et al.*, kp theory for two-dimensional transition metal dichalcogenide semiconductors. *2D Mater.* **2**, 022001 (2015).

[14] Laturia, A., Van de Put, M. L., and Vandenberghe, W. G., Dielectric properties of hexagonal boron nitride and transition metal dichalcogenides: from monolayer to bulk. *npj 2D Mater. and Appl.* **2**, 6 (2018).

[15] Jin, Z., Li, X., Mullen, J. T., and Kim, K. W., Intrinsic transport properties of electrons and holes in monolayer transition-metal dichalcogenides. *Phys. Rev. B* **90**, 045422 (2014).

[16] Rytova, N. S., Screened potential of a point charge in a thin film. *Proc. MSU, Phys., Astron.* **3**, 30 (1967) arXiv:1806.00976.

[17] Keldysh, L. V., Coulomb interaction in thin semiconductor and semimetal films. *JETP Lett.* **29**, 658 (1979) `http://www.jetpletters.ac.ru/ps/1458/article_22207.shtml`.

[18] Kira, M. and Koch, S. W., Many-body correlations and excitonic effects in semiconductor spectroscopy. *Prog. Quant. Electron.* **30**, 155 (2006).

[19] Malic, E., Dark excitons in transition metal dichalcogenides. *Phys. Rev. Mater.* **2**, 014002 (2018).

[20] Xiao, D., Liu, G.-B., Feng, W., Xu, X., and Yao, W., Coupled spin and valley physics in monolayers of MoS_2 and other group-VI dichalcogenides. *Phys. Rev. Lett.* **108**, 196802 (2012).

[21] Brem, S., Selig, M., Berghaeuser, G., and Malic E., Exciton relaxation cascade in two-dimensional transition metal dichalcogenides. *Sci. Rep.* **8**, 8238 (2018).

[22] Brem, S. *et al.*, Intrinsic lifetime of higher excitonic states in tungsten diselenide monolayers *Nanoscale* (2019), arXiv:1904.04729.

[23] Cho, Y. and Berkelbach, T. C., Environmentally sensitive theory of electronic and optical transitions in atomically thin semiconductors. *Phy. Rev. B* **97**, 041409 (2018).

[24] Ballif, C. *et al.*, Preparation and characterization of highly oriented, photoconducting WS_2 thin films. *Appl. Phys. A* **62**, 543 (1996).

[25] Berkelbach, T. C., Hybertsen, M. S., and Reichman, D. R., Theory of neutral and charged excitons in monolayer transition metal dichalcogenides. *Phys. Rev. B* **88**, 045318 (2013).

[26] Wang, G. *et al.*, Colloquium: Excitons in atomically thin transition metal dichalcogenides. *Rev. of Mod. Phys.* **90**, 021001 (2018).

[27] Aslan, O. B., Deng, M., and Heinz, T. F., Strain tuning of excitons in monolayer WSe_2. *Phys. Rev. B* **98**, 115308 (2018).
[28] Sidler, M. *et al.*, Fermi polaron-polaritons in charge-tunable atomically thin semiconductors. *Nature Phys.* **13**, 255 (2016).
[29] Plechinger, G. *et al.*, Trion fine structure and coupled spinvalley dynamics in monolayer tungsten disulfide. *Nature Commun.* **7**, 12715 (2016).
[30] Kulig, M. *et al.*, Exciton diffusion and halo effects in monolayer semiconductors. *Phys. Rev. Lett.* **120** (2018).